ACS APPLIED ENERGY MATERIALS

www.acsaem.org Article

Macroporous, Freestanding Birnessite $H_{0.08}MnO_2{\cdot}0.7H_2O$ Nanobelts/Carbon Nanotube Membranes for Wearable Zinc-Ion Batteries with Superior Rate Capability and Cyclability

Yanan Wang, Fei Ye, Zeyi Wu, Le Jiang, Lin Zhang, and Linfeng Hu*

Cite This: *ACS Appl. Energy Mater.* 2021, 4, 4138–4149 Read Online

ACCESS | Metrics & More | Article Recommendations | Supporting Information

ABSTRACT: Rechargeable aqueous zinc-ion batteries (ZIBs) are regarded as an ideal choice for next-generation energy-storage devices. Nevertheless, the ZIB performance is still far from satisfactory due to the lack of suitable cathode materials. In this work, we demonstrated excellent zinc-ion-storage behavior in proton-type birnessite $H_{0.08}MnO_2{\cdot}0.7H_2O$ nanobelts for the first time using a well-designed $H_{0.08}MnO_2{\cdot}0.7H_2O$/MWCNT composite membrane. Interestingly, our $H_{0.08}MnO_2{\cdot}0.7H_2O$ nanobelts with a very high aspect ratio (~30) facilitate the formation of abundant macropores of 0.5−5.0 μm size inside the as-constructed membrane, which provides an effective pathway for liquid electrolyte penetration during the long-term charge/discharge cycling. The resultant $H_{0.08}MnO_2{\cdot}0.7H_2O$/MWCNT composite membrane delivers a high Zn^{2+} diffusion coefficient of ~8.18×10^{-14} cm^2 s^{-1}, excellent rate capability, and long-term cyclability over 1000 cycles at 3.0 A g^{-1}. Our study not only reveals $H_{0.08}MnO_2{\cdot}0.7H_2O$ as a robust cathode material for aqueous zinc-ion batteries but also demonstrates a macropore-assisted binder-free strategy to realize next-generation energy-storage devices from layered nanostructures with a high aspect ratio.

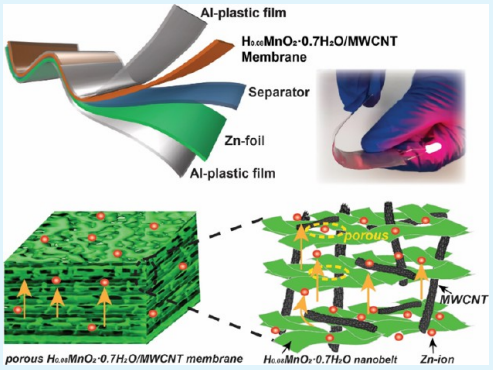

KEYWORDS: *freestanding membrane, birnessite $H_{0.08}MnO_2{\cdot}0.7H_2O$, macroporous structure, binder-free, aqueous zinc-ion battery*

INTRODUCTION

Metallic Zn has been considered as an ideal anode material for high-performance energy storage owing to its high abundance and low cost, high theoretical capacity (820 mA h·g^{-1}), low electrochemical potential (−0.762 V vs the standard hydrogen electrode), and low toxicity.[1−4] More intriguingly, a highly reversible Zn^{2+} storage can be easily realized in a Zn//cathode battery system using an aqueous, nonflammable electrolyte, which remarkably improves the battery safety and environmental friendliness.[5,6] These prominent advantages have directly driven rapid developments in rechargeable zinc-ion batteries (ZIBs) recently. Unfortunately, the surface-charge density of divalent Zn^{2+} is twice more than that of Li^+, leading to much stronger electrostatic interactions between Zn^{2+} and the lattice framework of the electrode materials and sluggish diffusion kinetics.[7] Therefore, the development of ZIBs is still hindered by the lack of suitable cathode materials possessing sufficient specific-energy density and long-term cycle life.

The key component of the ZIB cathode is the active material for Zn-ion storage and transport. Manganese-based oxides, including α-MnO_2,[2] β-MnO_2,[8] γ-MnO_2,[9] and spinel-type MnO_2,[10,11] have been considered as very promising candidates for the active material in rechargeable ZIBs. Especially, birnessite-type manganese oxides consist of layered stacking of edge-sharing [MnO_6] octahedra along the *c*-axis, with water molecules accommodated in the interlayer space, providing a natural two-dimensional tunnel for Zn^{2+} insertion and extraction.[12,13] Compared to hollandite manganese oxides with a tunnel structure,[14−16] there are far fewer reports on the Zn ion battery performance using birnessite as the cathode. Most recently, some Mn-based birnessites such as δ-MnO_2,[17] K^+-based $K_{1.33}Mn_8O_{16}$,[18] and Cu^{2+}-based Bi-δ-MnO_2[19] have been developed as novel cathode materials for ZIBs. Despite being an important birnessite, proton-type $H_{0.08}MnO_2{\cdot}0.7H_2O$[20] has never been studied as a ZIB cathode till date. It should be interesting to obtain a fundamental understanding of the intrinsic zinc-ion-storage mechanism in layered $H_{0.08}MnO_2{\cdot}0.7H_2O$ to enrich the birnessite-type manganese oxides as advanced ZIB cathode materials.

On the other hand, the traditional cathode for aqueous ZIBs is often fabricated by mixing active materials with polymer binders and conductive carbon additives and then coating the

Received: February 15, 2021
Accepted: March 19, 2021
Published: March 31, 2021

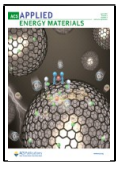

https://doi.org/10.1021/acsaem.1c00464
ACS Appl. Energy Mater. 2021, 4, 4138–4149

slurry onto current collectors.[21,22] The introduction of a polymer binder not only severely blocks the transport of Zn ions at the current collector/active material interface but also results in the cracking and exfoliation of active materials during deformation.[23−25] In recent years, the rational design of binder-free and current collector-free cathodes for aqueous ZIBs has attracted great attention. However, most of the binder-free cathodes thus far are densely packed thin films constructed from the ordered stacking of two-dimensional nanostructures.[26] If one can introduce abundant micrometer-sized macropores into these freestanding thin films, enhanced battery performance would be realized owing to the efficient permeation of the liquid electrolyte and accommodation of the electrode volumetric changes during the charge/discharge cycle. Unfortunately, to the best of our knowledge, this merit has rarely been achieved and still remains a challenge.

Herein, we demonstrated excellent zinc-ion-storage behavior in a binder-free $H_{0.08}MnO_2{\cdot}0.7H_2O$ membrane for the first time through a macropore-assisted strategy. Long $H_{0.08}MnO_2{\cdot}0.7H_2O$ nanobelts with a high aspect ratio (∼30) were employed as ideal building blocks to construct flexible membranes by a vacuum-assisted filtration strategy, with the controllable addition of conductive multiwalled carbon nanotubes (MWCNTs) (Scheme 1). Interestingly, the self-stacking process of these $H_{0.08}MnO_2{\cdot}0.7H_2O$ nanobelts and CNTs generally resulted in an interconnected 0.5−5.0 μm macroporous architecture in the hybrid membrane, which provides an effective pathway for the rapid penetration of the liquid electrolyte and can be well maintained during the long-term charge/discharge cycling. The resultant $H_{0.08}MnO_2{\cdot}0.7H_2O$/MWCNT macroporous membrane cathode delivered a high Zn^{2+} diffusion coefficient of ∼8.18×10^{-14} cm^2 s^{-1}, excellent rate capability, and stable cyclability over 1000 cycles at 3.0 A g^{-1}, which are remarkably superior to those of conventional Mn-based compounds.

Scheme 1. Schematic Illustration of the Fabrication Process of Macroporous, Freestanding $H_{0.08}MnO_2{\cdot}0.7H_2O$/MWCNT Membrane

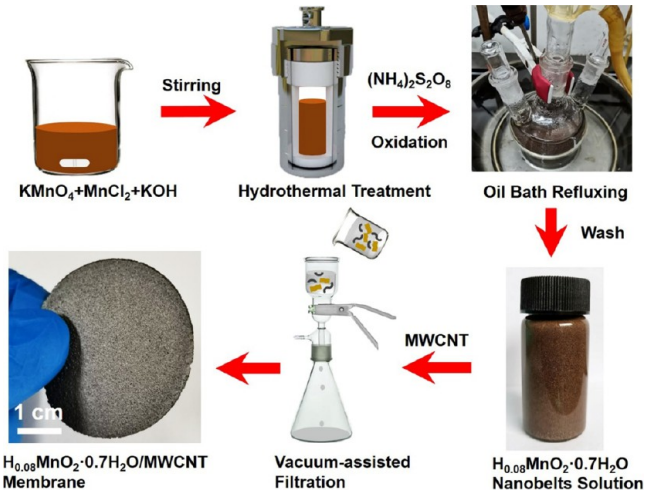

RESULTS AND DISCUSSION

Freestanding $H_{0.08}MnO_2{\cdot}0.7H_2O$/MWCNT Hybrid Membrane. The $H_{0.08}MnO_2{\cdot}0.7H_2O$ sample was prepared from the $K_{0.33}MnO_2{\cdot}0.5H_2O$ birnessite precursor by the same ion-exchange method as previously reported.[20] The corresponding X-ray diffraction (XRD) pattern confirms the high purity with sharp (001) diffraction peaks (Figure 1a), indicating a basic d-spacing of 7.3 Å for the layered crystal. All the diffraction peaks match well with the one reported by Liu et al. and could be readily indexed as a primitive hexagonal cell ($a = b = 0.2843$ nm; $c = 0.7311$ nm).[20] Thus, the structural and compositional data of our sample are comparable to those reported for the proton-type birnessite. Figure 1b schematically illustrates the in-plane crystal structure of $H_{0.08}MnO_2{\cdot}0.7H_2O$ birnessite. Based on previous studies,[20,26] the layered $H_{0.08}MnO_2{\cdot}0.7H_2O$ crystal was obtained by the deintercalation of K^+ ions in the $K_{0.33}MnO_2{\cdot}0.5H_2O$ precursor, and the protons (H_3O^+ form) just stay in the interlayer gallery through weak interactions between the lattice oxygen atoms of the [MnO_6] polyhedron.[20] Scanning electron microscopy (SEM) and transmission electron microscopy (TEM) observations show a typical belt-like morphology with a width of 0.3−1.0 μm and a length over 10 μm (Figure 1b), suggesting a very high aspect ratio (length/width) of 10−30. The corresponding selected-area electron diffraction (SAED) pattern obtained for an individual nanobelt exhibits sharp, hexagonally arranged diffraction spots, which are attributable to the in-plane (*ab* plane) reflections of birnessite[20] (Figure 1c). The high-resolution TEM (HRTEM) image exhibits resolved 1.4 and 2.5 Å spacings of the lattice fringes, agreeing well with the expected separation of the (110) and (100) planes, respectively (Figure 1d). The negatively charged surface of the nanobelts was demonstrated by zeta potential measurements (−30.5 mV, Figure S1).

Benefiting from their high aspect ratio and intrinsic flexibility, the as-prepared $H_{0.08}MnO_2{\cdot}0.7H_2O$ nanobelts are found to be easily self-woven into a flexible, freestanding membrane during the vacuum-assisted filtration of this suspension. Considering that layered birnessite generally suffers from low electronic conductivity, which significantly hinders the electron transport when it is used as a battery electrode, we tried to incorporate conductive MWCNTs into this membrane. Accordingly, a stable colloidal suspension was readily prepared through homogeneously mixing $H_{0.08}MnO_2{\cdot}0.7H_2O$ nanobelt aqueous suspension (4.25 mg mL^{-1}) and MWCNT suspension in *N*-methylpyrrolidone (NMP, 0.5 mg mL^{-1}) at a volume ratio of 1:2, followed by an ultrasonic treatment. Then, the $H_{0.08}MnO_2{\cdot}0.7H_2O$ nanobelts and MWCNTs were self-woven together to produce a freestanding membrane during vacuum-assisted filtration (Scheme 1). The optimal content of MWCNTs in the composite membrane is estimated as ∼20 wt %. The lower mass ratio of conductive MWCNTs than this threshold value gives rise to a membrane sample with a high electric resistance[27] (Figure 2). A too high mass ratio of MWCNTs generally causes cracks in the membrane and drastically damages their mechanical properties. The as-obtained membrane exhibits excellent flexibility and can be easily rolled up by hand (Figure S2). The XRD pattern of the composite membrane presents the characteristic peaks of $H_{0.08}MnO_2{\cdot}0.7H_2O$, which are in good agreement with that of the powder sample, except for the additional peak at $2\theta = 24.5°$ due to the MWCNT diffraction peak (Figure 3a, inset shows 10 times magnified XRD patterns from 30−70° and a highly flexible picture). More importantly, from the top-view and cross-sectional SEM images, it is observed that our composite membrane is rich with numerous macropores of 0.5−5 μm size (Figure 3b−d). This further confirmed that the

https://doi.org/10.1021/acsaem.1c00464
ACS Appl. Energy Mater. 2021, 4, 4138−4149

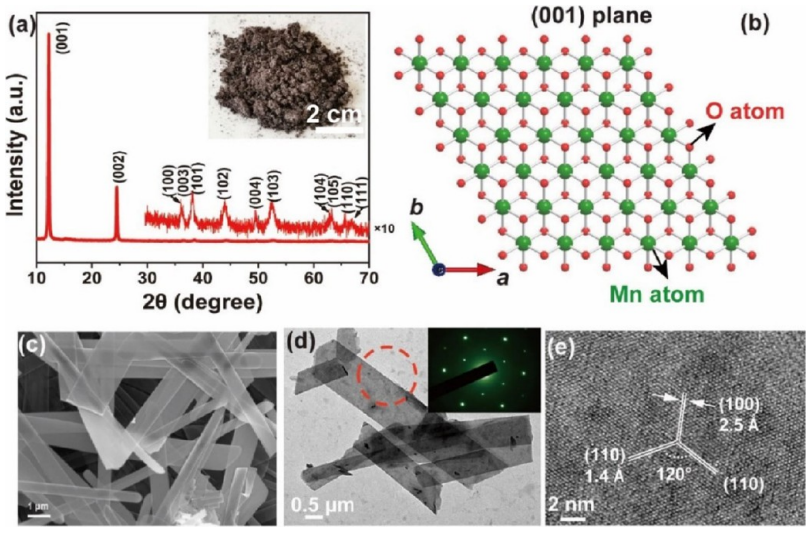

Figure 1. (a) Powder XRD pattern and (b) top view of layered $H_{0.08}MnO_2{\cdot}0.7H_2O$ birnessite along the *c*-axis. (c) Typical SEM, (d) TEM, and (e) HRTEM images of the as-prepared $H_{0.08}MnO_2{\cdot}0.7H_2O$ nanobelts. Inset in (d) shows the corresponding SAED pattern obtained from an individual nanobelt.

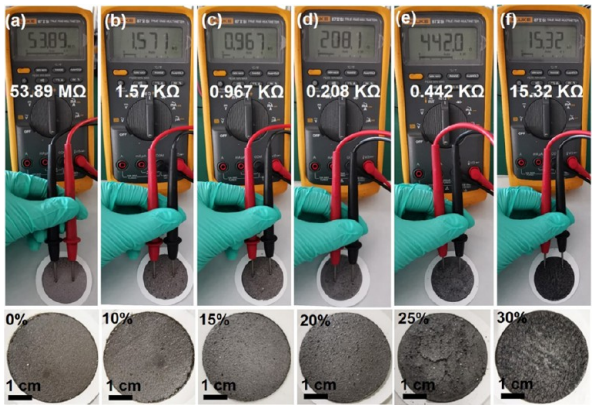

Figure 2. (a–f) Electric resistance measurement of the $H_{0.08}MnO_2{\cdot}0.7H_2O$/MWCNT composite membrane with various MWCNT contents from 0 to 30 wt %. As the content of MWCNTs is increased up to a high value of 30%, the membrane breaks into many small pieces, resulting in the drastic increase of resistance.

pure $H_{0.08}MnO_2{\cdot}0.7H_2O$ membrane without MWCNT addition shows a similar macroporous cross-section as that of the composite one (Figure S3). Accordingly, we consider that the large number of macropores should have originated from the disordered stacking of our $H_{0.08}MnO_2{\cdot}0.7H_2O$ nanobelts with a very high aspect ratio and intrinsic flexibility. Note that the surface of the $H_{0.08}MnO_2{\cdot}0.7H_2O$/MWCNT hybrid membrane is evidently rough and porous than that of the pure $H_{0.08}MnO_2{\cdot}0.7H_2O$ one, indicating that the introduction of MWCNTs facilitates the formation of a porous surface due to the remarkable morphology/size difference between the $H_{0.08}MnO_2{\cdot}0.7H_2O$ nanobelts and MWCNTs. In addition, the cross-sectional energy-dispersive spectral composition maps shown in Figure 3f–h demonstrate the almost uniform distribution of MWCNTs without apparent agglomeration. This result indicates a very dense contract between the $H_{0.08}MnO_2{\cdot}0.7H_2O$ nanobelts and MWCNTs in the hybrid architecture, which can provide efficient pathways for electron transport through the $H_{0.08}MnO_2{\cdot}0.7H_2O$ nanobelt/MWCNT interface.

X-ray photoelectron spectroscopy (XPS) characterization was further conducted to confirm the C, Mn, and O valence states of the hybrid membrane surface (Figure S4). One can see that the high-resolution C 1s spectrum (Figure 3i) can be fitted into three groups of spin–orbit peaks, corresponding to C–C (284.4 eV), C–O (285.6 eV), and C═O (288.4 eV),[28−30] respectively. For the Mn 2p spectrum (Figure 3j), four groups of spin–orbit resolved peaks can be well-fitted, corresponding to Mn^{3+} ($2p_{1/2}$, 653.8 eV), Mn^{4+} ($2p_{1/2}$, 652.6 eV),[31] Mn^{3+} ($2p_{3/2}$, 643.5 eV), and Mn^{4+} ($2p_{3/2}$, 642.5 eV),[32,33] respectively, suggesting a molar ratio of ∼11.5:1 for Mn^{4+}/Mn^{3+} in the sample. Thus, the Mn valence state in this membrane is 3.92, which agrees well with the reported literature.[20] In addition, three peaks can be resolved from the convoluted O 1s spectrum corresponding to O–Mn (529.2 eV), –OH (531.6 eV), and H–O–H (532.9 eV) (Figure 3k).[34] The mechanical properties of the $H_{0.08}MnO_2{\cdot}0.7H_2O$/MWCNT membrane with a maximum tensile force of 2.54 N and an elongation at break of 1.6% are comparable with the results of our previous work (Figure S5).[26] Thermogravimetric analysis (TGA) was utilized to further evaluate the thermal stability of the $H_{0.08}MnO_2{\cdot}0.7H_2O$/MWCNT membrane (Figure S6). The mass loss ratio of 12.0% at the temperature range of 30–300 °C and 29.1% (300–900 °C) should be ascribed to the removal of coordinated water and MWCNT in our hybrid membrane, respectively, which is consistent with the reported proton-type birnessite.[20]

Electrochemical Properties and Mechanism. Benefiting from the merits of efficient Zn ion diffusion and the accommodation of volumetric changes of electrodes during the charge/discharge cycle, we consider that our macroporous, binder-free and current collector-free membrane is very promising for ZIB electrode application. Subsequently, the as-constructed $H_{0.08}MnO_2{\cdot}0.7H_2O$/MWCNT membrane was punched into discs (Φ = 15 mm; the mass loading ∼2.0 mg cm^{-2}) and assembled into typical coin-type cells using a zinc foil anode, a glass fiber (GF) separator, and a 2 M $ZnSO_4$/0.2 M $MnSO_4$ aqueous electrolyte. The cyclic voltammetry (CV) curves of $H_{0.08}MnO_2{\cdot}0.7H_2O$/MWCNT cathodes at various scan rates demonstrate the typical electron transfer process

https://doi.org/10.1021/acsaem.1c00464
ACS Appl. Energy Mater. 2021, 4, 4138–4149

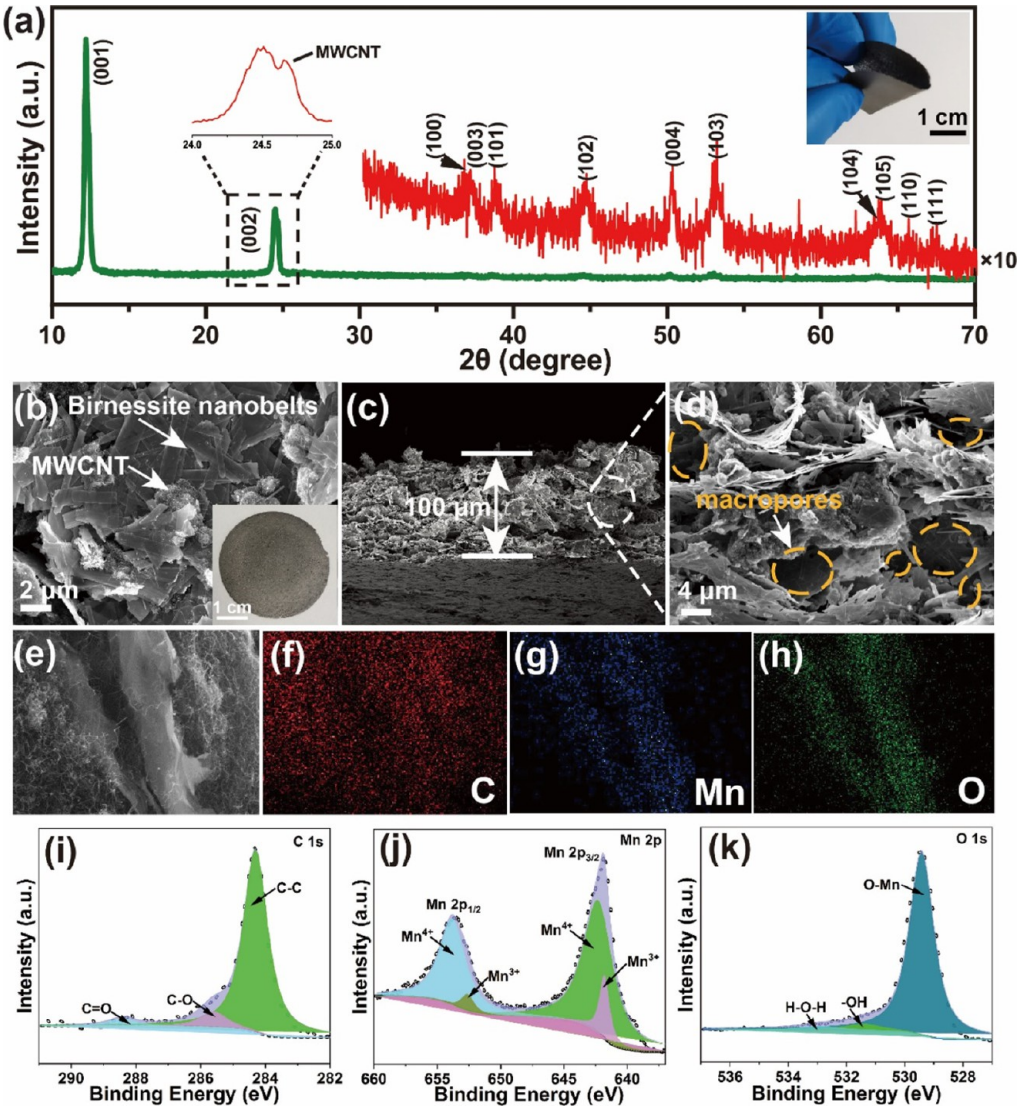

Figure 3. (a) XRD pattern of the $H_{0.08}MnO_2{\cdot}0.7H_2O$/MWCNT hybrid membrane. (b) Top-view image, (c) cross-sectional SEM image, and (d) enlarged SEM images to show a large number of macropores inside the membrane and also on the membrane surface. (e) Typical cross-sectional SEM images of the $H_{0.08}MnO_2{\cdot}0.7H_2O$/MWCNT membrane and the corresponding elemental mapping of (f) C, (g) Mn, and (h) O elements. (i–k) C 1s, Mn 2p, and O1s XPS spectra of the hybrid membrane, respectively.

between 1.0 and 1.9 V (vs Zn/Zn^{2+}) (Figure 4a). A pair of cathodic peaks at around 1.37 and 1.25 V are properly related to the stepwise intercalation of H^+ and Zn^{2+} into the $H_{0.08}MnO_2{\cdot}0.7H_2O$ lattice, respectively. The consequent anodic peaks at 1.56 and 1.62 V can be ascribed to the extraction of H^+ and Zn^{2+}, according to previous reports, respectively.[35,36] The linear fit of relationship between the logarithm (log) peak current and log scan rate indicates that the slopes of the anodic and cathodic peaks are 0.74 (peak 1), 0.66 (peak 2), 0.63 (peak 3), and 0.69 (peak 4), respectively (Figure 4b). This result demonstrates that the charge/discharge process of the $H_{0.08}MnO_2{\cdot}0.7H_2O$/MWCNT membrane electrode is affected by both ion diffusion and capacitive-controlled capacity, and the former plays the dominant role. Further quantitative analysis is utilized to separate the diffusion and capacitive-controlled capacity. The contribution of the capacitor current (green region) is separated from the total current, that is, 34.7, 40.9, 45.2, 49.6, and 51.2% at various scan rate ranges from 0.1 to 1.0 mV s^{-1} (Figure 4c, d), further suggesting that the battery-type effect plays a major role in the capacity contribution during the various scan rates. The second to fourth cycle galvanostatic discharge−charge (GDC) voltage profiles of the membrane cathode are shown in Figure 4b. One can see that there are two voltage plateaus at around 1.4 and 1.3 V, corresponding to the H^+ and Zn^{2+} intercalation process, respectively, which is well consistent with the abovementioned CV curves. A similar phenomenon has also been reported previously based on various MnO_2 cathodes.[26,37]

We further compare the electrochemical performance difference between the binder-free membrane cathode and the binder-rich powder form. Note that the $H_{0.08}MnO_2{\cdot}0.7H_2O$ powder cannot be directly obtained by the conventional filtration process due to its self-woven behavior, and other methods such as solvent evaporation generally leads to drastic agglomeration of the nanobelts. However, we found that the $H_{0.08}MnO_2{\cdot}0.7H_2O$ powder sample can be easily prepared by a freeze-drying route. Then, a binder-rich $H_{0.08}MnO_2{\cdot}0.7H_2O$/PVDF counterpart electrode was fabricated by mixing $H_{0.08}MnO_2{\cdot}0.7H_2O$ powder and poly(vinylidene fluoride) (PVDF) binder/carbon conductive

https://doi.org/10.1021/acsaem.1c00464
ACS Appl. Energy Mater. 2021, 4, 4138−4149

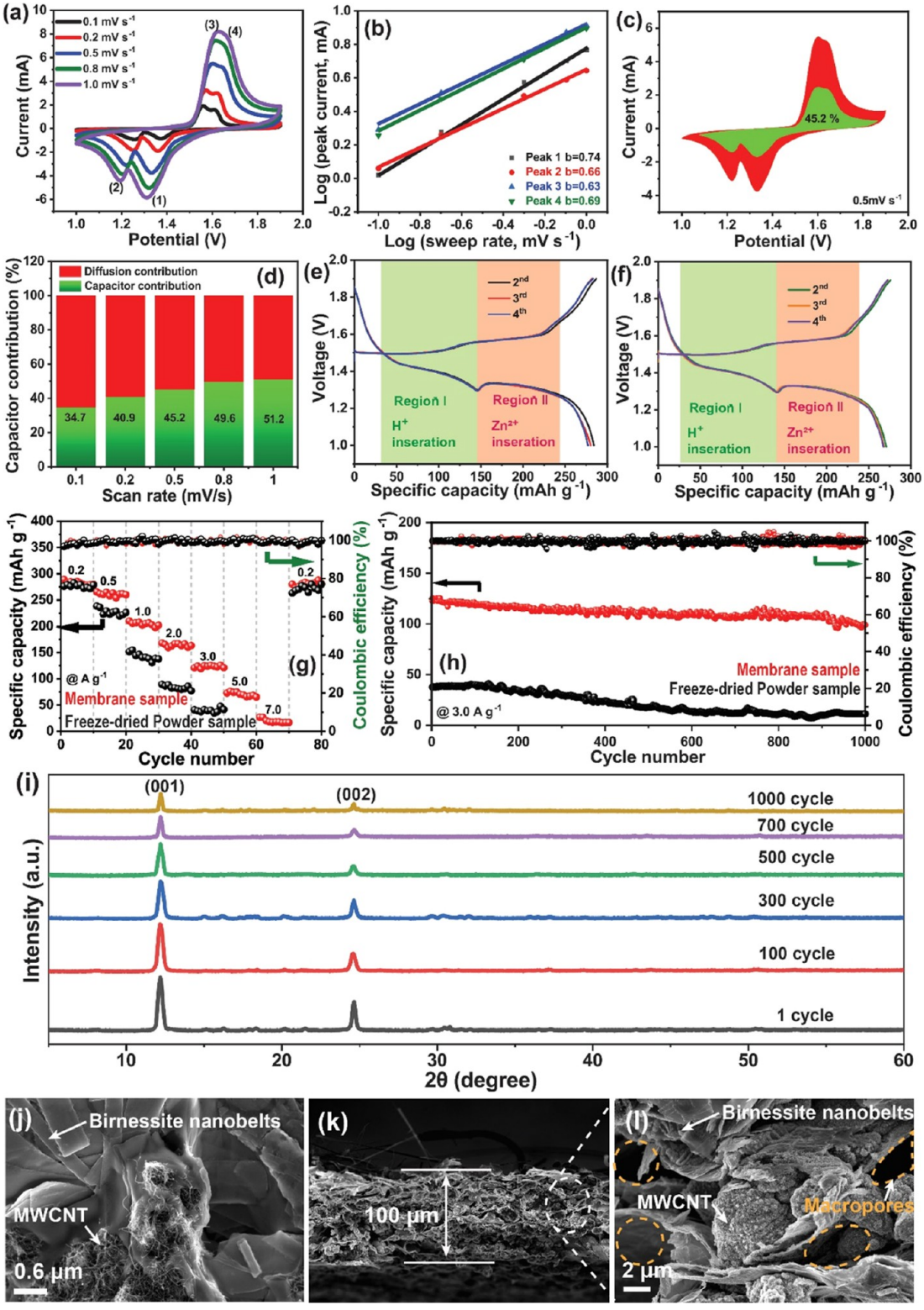

Figure 4. (a) CV profile of the $H_{0.08}MnO_2{\cdot}0.7H_2O$/MWCNT membrane cathode at various scan rates. (b) Logarithmic dependence of peak current density and scan rate of the $H_{0.08}MnO_2{\cdot}0.7H_2O$/MWCNT membrane-based ZIB in the CV test. (c) CV profile scanned at 0.5 mV s^{-1} and the corresponding pseudocapacitive contribution (green-colored area). (d) Pseudocapacitive contribution (green region) to the total current at different sweep rates. The second to fourth cycle GDC profiles of the (e) $H_{0.08}MnO_2{\cdot}0.7H_2O$/MWCNT membrane and (f) $H_{0.08}MnO_2{\cdot}0.7H_2O$/PVDF powder cathode. (g) Rate capability for the $H_{0.08}MnO_2{\cdot}0.7H_2O$/MWCNT membrane and $H_{0.08}MnO_2{\cdot}0.7H_2O$/PVDF powder cathode at various current densities, ranging from 0.2 to 7 A g^{-1}, respectively. (h) Cycle performance and the corresponding Coulombic efficiency of the $H_{0.08}MnO_2{\cdot}0.7H_2O$/MWCNT membrane and the $H_{0.08}MnO_2{\cdot}0.7H_2O$/PVDF powder cathode in the range 1−1.9 V at 3.0 A g^{-1}, respectively. (i) XRD patterns of the $H_{0.08}MnO_2{\cdot}0.7H_2O$/MWCNT membrane after different GDC cycles at the charge voltage of 1.9 V. (j) Top view, (k) cross-sectional SEM image, and (l) enlarged cross-sectional SEM image of the $H_{0.08}MnO_2{\cdot}0.7H_2O$/MWCNT cathode undergoing 1000 cycles.

https://doi.org/10.1021/acsaem.1c00464
ACS Appl. Energy Mater. 2021, 4, 4138−4149

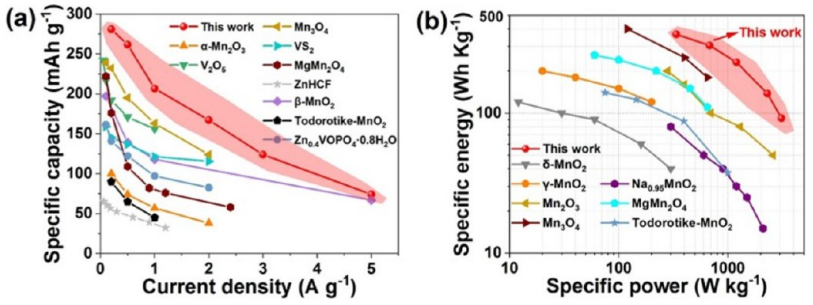

Figure 5. (a) Comparison of the rate capability of our work and the conventional cathode material of aqueous ZIBs reported recently.[8,41−48] (b) Ragone plot of our $H_{0.08}MnO_2{\cdot}0.7H_2O$/MWCNT membrane cathode and other Mn-based cathodes.

additives as a slurry coating onto current collectors. Although no evident difference is detected from the GDC voltage profiles (Figure 4c), these two samples deliver dramatic differences in rate capability and long-term cyclability. The $H_{0.08}MnO_2{\cdot}0.7H_2O$/MWCNT membrane electrode exhibits excellent rate capability with specific discharge capacities of 276.3, 263.5, 206.7, 167.2, 123.9, 74.2, and 20.3 mA h g^{-1} at current densities of 0.2, 0.5, 1.0, 2.0, 3.0, 5.0, and 7.0 A g^{-1}, respectively (Figures 4d and S7). When the current density returns back to 0.2 A g^{-1}, the reversible capacity recovers back to 277.6 mA h g^{-1}. In contrast, the freeze-dried $H_{0.08}MnO_2{\cdot}0.7H_2O$ powder cathode displays rather poor rate capabilities at various current rates, that is, 273.3, 219.8, 138.5, 80.9, and 37.1 mA h g^{-1}, at the current densities of 0.2, 0.5, 1.0, 2.0, and 3.0, respectively (Figure 4d). In addition, the membrane-based ZIB delivers an outstanding long-term cyclability with an initial specific capacity of 124.2 mA h g^{-1} and retained 80.8% of the initial specific capacity after 1000 GDC cycles at a high rate of 3.0 A g^{-1} with an average Coulombic efficiency around 100%. However, the freeze-dried $H_{0.08}MnO_2{\cdot}0.7H_2O$ counterpart just shows a very low initial specific capacity of 38.4 mA h g^{-1} and exhibits 31.4% capacity retention after 1000 GDC cycles, which is significantly inferior to that of our membrane cathode sample (Figure 4e). Moreover, similar trends of cycle performance were also observed at a lower rate of 0.2 A g^{-1} (Figures S8 and S9). *Ex situ* XRD characterization was further used to check the structural stability of our $H_{0.08}MnO_2{\cdot}0.7H_2O$/MWCNT membrane cathode (Figure 4f). Evidently, the XRD pattern of the membrane cathode remains unchanged even after 1000 GDC cycles, and almost no considerable intensity changes are observed at 500 cycles, demonstrating its robust phase stability. SEM observations also identify stable morphology during the long-term charge/discharge cycling (Figure 4g−i). It is clear that our layered $H_{0.08}MnO_2{\cdot}0.7H_2O$ nanobelts display initial belt-like morphology and high aspect ratio, undergoing 1000 cycles. More importantly, the macropores inside the $H_{0.08}MnO_2{\cdot}0.7H_2O$/MWCNT membrane are not collapsed during the long cycle process, which should be the reason for the as-observed excellent long-term cyclability of the battery. Moreover, the SEM images of the postcycled electrolyte show the formation of a rough layer on the surface of the electrodes, which assumes a parasitic reaction that involves the deposition of $Zn(OH)_2ZnSO_4{\cdot}5H_2O$.

In general, $MnSO_4$ is normally added to compensate for the partial dissolution of manganese dioxide during the charge process.[38−40] We further detect the influence of $MnSO_4$ addition on the battery's long-term cyclability. The assembled $H_{0.08}MnO_2{\cdot}0.7H_2O$/MWCNT//Zn cell without $MnSO_4$ in the electrolyte system exhibits an initial specific capacity of 120.1 mA h g^{-1} and 35.1% capacity retention after 1000 cycles (Figure S10), demonstrating that the presence of $MnSO_4$ is very important for the cycling stability of cells. However, it should be noteworthy that such a long-term stability was not observed in the freeze-dried $H_{0.08}MnO_2{\cdot}0.7H_2O$ counterpart without a macroporous structure, even with the addition of $MnSO_4$ (Figure S8). Accordingly, it is rational that the macroporous structure plays a decisive role in the aforementioned superior cyclability.

Figure 5a compares the rate capability of ZIBs assembled with our $H_{0.08}MnO_2{\cdot}0.7H_2O$/MWCNT membrane electrode and other conventional electrodes reported recently.[8,41−48] Remarkably, the specific capacity of our sample surpassed conventional cathode materials at various current densities from 0.1 to 5 A g^{-1}. Benefiting from the superior rate capability, the energy densities of our membrane-based ZIBs, as shown in Ragone plots (Figure 5b), are 368.3 W h·kg^{-1} at 300 W·kg^{-1} and 160 W h·kg^{-1} at 2150 W·kg^{-1} (based on the weight of $H_{0.08}MnO_2{\cdot}0.7H_2O$ only). This performance is much superior to that of the recently reported Mn-based ZIBs, including α-,[2] β-,[8] δ-,[49] γ-MnO_2,[9] Mn_2O_3,[42] Mn_3O_4,[44] $MgMn_2O_4$,[45] Todorotike-MnO_2,[47] $Na_{0.95}MnO_2$,[50] and so forth.

Ex situ XRD characterization was performed to understand the Zn^{2+} storage mechanism and kinetics of our freestanding $H_{0.08}MnO_2{\cdot}0.7H_2O$/MWCNT membrane cathode more clearly (Figure 6a−c). In detail, the (001) diffraction peak shifts gradually from 12.1° toward 12.3° during the discharging process, implying a reduction in the interlayer distance of $H_{0.08}MnO_2{\cdot}0.7H_2O$ that is induced by the strong electrostatic interaction between the MnO_6 octahedral sheets and the intercalated zinc ions.[51,52] Besides, the (001) peaks could return to their original positions after the following charging process, reflecting a reversible process of insertion/extraction of zinc ions without the destruction of $H_{0.08}MnO_2{\cdot}0.7H_2O$. Furthermore, as in the discharging process from A to D, two-stage discharge plateaus appear clearly. The first stage of discharge to ∼1.3 V (consisting region I, green color in Figure 4f) is supposed to be dominated by the insertion of H^+ ($H_2O \leftrightarrow H^+ + OH^-$; $H_{0.08}MnO_2{\cdot}0.7H_2O + xH^+ + xe^- \leftrightarrow H_{(0.08+x)}MnO_2{\cdot}0.7H_2O$). With a sustained decrease of H^+ concentration, the second discharge platform arises (consisting region II, red color in Figure 4f), which is mainly caused by the insertion reaction of Zn^{2+} ($H_{0.08+x}MnO_2{\cdot}0.7H_2O + yZn^{2+} + 2ye^- \leftrightarrow Zn_yH_{0.08+x}MnO_2{\cdot}0.7H_2O$ ($0 < y < 1$)). Meanwhile, some new obvious peaks at 7.9 and 16.2° and other weak peaks (highlighted with green stars) are generated from ∼1.3 V, which match well with those of zinc hydroxide sulfate hydrate $3Zn(OH)_2{\cdot}ZnSO_4{\cdot}5H_2O$, JCPDS 78-0246 ($4Zn^{2+} + 6OH^- + SO_4^{2-} + 5H_2O \leftrightarrow 3Zn(OH)_2{\cdot}ZnSO_4{\cdot}5H_2O$).[53] The presence

https://doi.org/10.1021/acsaem.1c00464
ACS Appl. Energy Mater. 2021, 4, 4138−4149

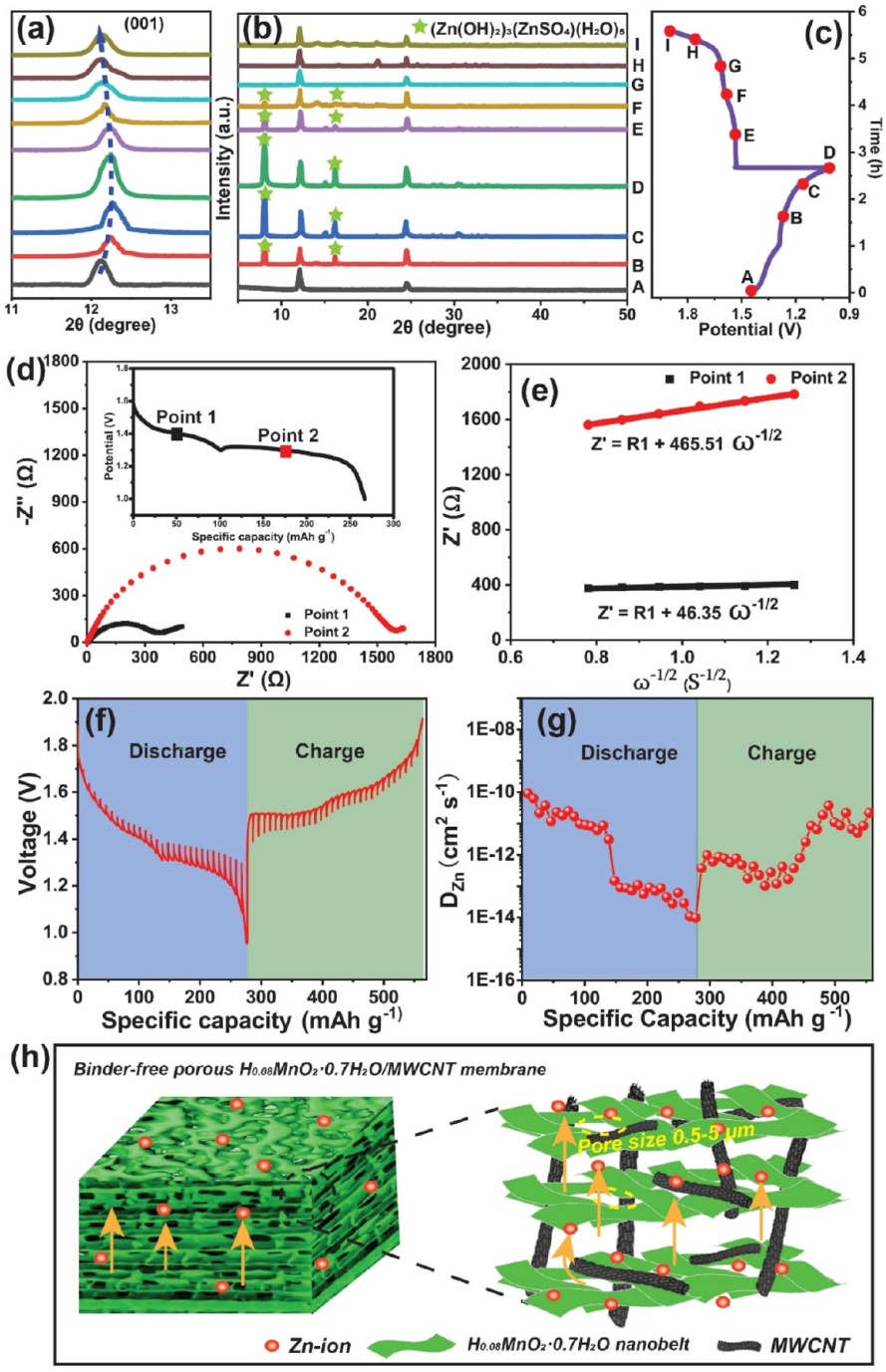

Figure 6. (a–c) *Ex situ* XRD pattern of the $H_{0.08}MnO_2{\cdot}0.7H_2O$/MWCNT membrane cathode at different charge/discharging states. (d) Zn^{2+} diffusion coefficient analysis based on the measured EIS spectrum at the corresponding points on the discharge platform (inset). (e) Dependence of Z' and $\omega^{-1/2}$ on the low-frequency region according to the EIS tests. (f) GITT profile of the $H_{0.08}MnO_2{\cdot}0.7H_2O$/MWCNT battery. (g) Calculated corresponding ion-diffusion coefficients of our $H_{0.08}MnO_2{\cdot}0.7H_2O$/MWCNT membrane cathode at different discharge/charge stages. (h) Schematic illustration of the fast Zn^{2+}-ion transport in porous $H_{0.08}MnO_2{\cdot}0.7H_2O$/MWCNT frameworks.

of $3Zn(OH)_2{\cdot}ZnSO_4{\cdot}5H_2O$ suggests the availability of sufficient amount of OH^- groups in the electrolyte, confirming the reversible H^+ intercalation reaction.[2] During the next charging process (from D to I), the sharp peaks of $3Zn(OH)_2{\cdot}ZnSO_4{\cdot}5H_2O$ gradually weaken until they disappear at 1.6 V (G). Note that the final XRD pattern (I) was well consistent with the initial one (A). This result demonstrates that the Zn^{2+}-storage mechanism in layered $H_{0.08}MnO_2{\cdot}0.7H_2O$ is followed by a typical intercalation/de-intercalation mechanism rather than a conversion mechanism.

Electrochemical impedance spectroscopy (EIS) measurements, including the typical Nyquist spectra tested at first (Point 1) and second (Point 2) discharge platforms (Figure 6d) and the Z' versus $\omega^{-1/2}$ plots (Figure 6e), were further conducted to identify the H^+ and Zn^{2+} diffusion capability at the discharge platform of our $H_{0.08}MnO_2{\cdot}0.7H_2O$/MWCNT membrane. The calculated platform diffusion coefficients of H^+ and Zn^{2+} can reach up to 8.26×10^{-12} (the first discharge platform at 1.37 V) and 8.18×10^{-14} cm^2 s^{-1} (the second platform at 1.25 V), respectively, which is comparable with the

https://doi.org/10.1021/acsaem.1c00464
ACS Appl. Energy Mater. 2021, 4, 4138–4149

Table 1. Comparison of *DZn2+* at the Discharge Plateau of Various Cathode Materials in ZIBs

cathode material	electrolyte	*DZn2+* at discharge plateau ($cm^2\ s^{-1}$)	refs
$H_{0.08}MnO_2{\cdot}0.7H_2O$/MWCNTs	2 M $ZnSO_4$ + 0.2 M $MnSO_4$	8.18×10^{-14}	This work
α-MnO_2	2 M $ZnSO_4$ + 0.24 M $MnSO_4$	7.97×10^{-15}	11
MnO_2/MWCNTs	2 M $ZnSO_4$ + 0.2 M $MnSO_4$	1.93×10^{-14}	26
PANI-intercalated MnO_2	2 M $ZnSO_4$ + 0.1 M $MnSO_4$	7.35×10^{-14}	54
β-MnO_2@CC	3 M $ZnSO_4$ + 0.1 M $MnSO_4$	6.5×10^{-16}	57
Ti−MnO_2 NWs	3 M $Zn(CF_3SO_3)_2$ + 0.1 M $Mn(CF_3SO_3)_2$	5.0×10^{-15}	32
MnO_2	2 M $ZnSO_4$ + 0.1 M $MnSO_4$	1.0×10^{-14}	58

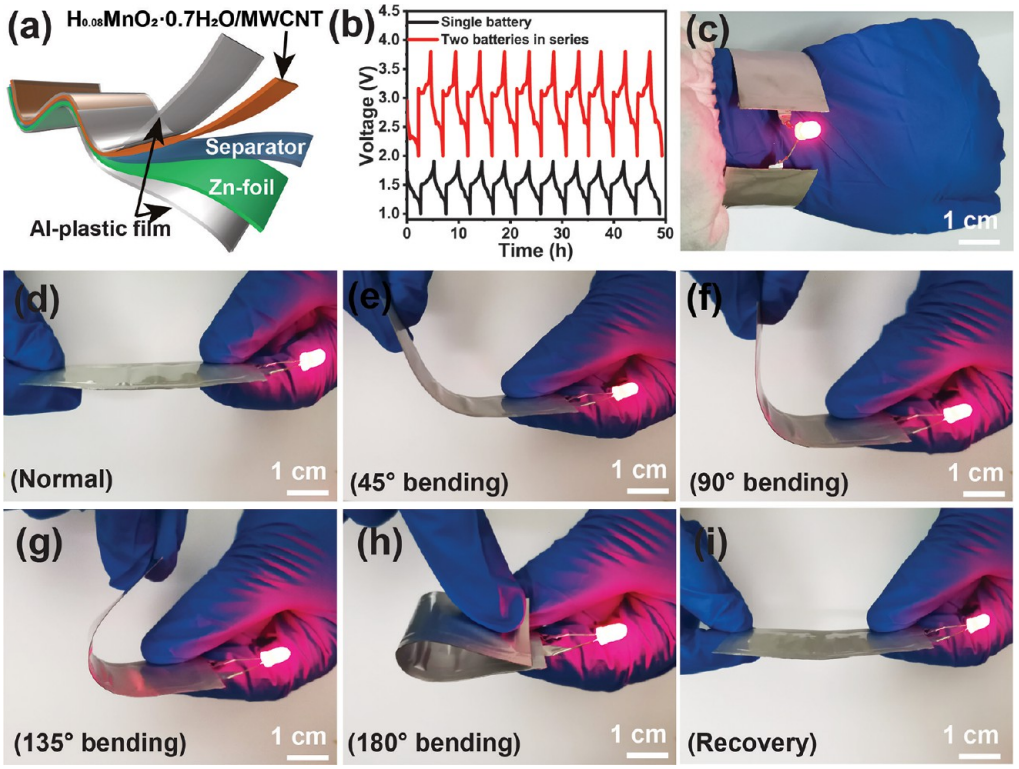

Figure 7. (a) Schematic of the sandwich structure of the constructed flexible battery. (b) GDC curves of a single battery and of two batteries connected in series at 0.2 A/g. (c) Photograph of the as-assembled flexible battery wrapped around the wrist and light up of a red LED indicator. (d–i) Flexible battery lighting up a red LED indicator at different bending angles.

highest value in the recent reports on δ-MnO_2 cathode for ZIBs.[54] As a comparative experiment, the freeze-dried $H_{0.08}MnO_2{\cdot}0.7H_2O$ powder sample delivers much lower H^+ and Zn^{2+} diffusion coefficients of 1.07×10^{-12} and 2.35×10^{-14} $cm^2\ s^{-1}$, respectively (Figure S11). It is clear that the apparent diffusion coefficients of H^+ and Zn^{2+} in our membrane cathode sample are 7.7 and 3.5 times higher than that of the powder cathode sample, respectively. Moreover, the galvanostatic intermittent titration technique (GITT) was further utilized to estimate the ion diffusion coefficient (*DGITT*, $cm^2\ s^{-1}$) in our $H_{0.08}MnO_2{\cdot}0.7H_2O$/MWCNT membrane cathode (Figure 6f,g),[55,56] which displays the H^+ and Zn^{2+} diffusion coefficients of $\sim 8.3 \times 10^{-12}$ and $\sim 8.1 \times 10^{-14}$ $cm^{-2}\ s^{-1}$ at the two discharge plateaus of 1.9–1.3 and 1.3–1.0 V (discharge region), respectively. The GITT results are well consistent with the above EIS measurement-tested diffusion coefficients of H^+ and Zn^{2+}, suggesting a rapid ion diffusion ability in our $H_{0.08}MnO_2{\cdot}0.7H_2O$/MWCNT cathode. It is noteworthy that the Zn^{2+} diffusion ability of our sample is also much higher than that of the other recently reported cathode materials (Table 1), further demonstrating the intrinsic advantage of the macroporous structure inside the freestanding cathode toward reversible Zn ion insertion/extraction. As schematically illustrated in Figure 6h, the as-observed Zn-ion-diffusion ability should be ascribed to the following factors: (a) the macroporous structure of the membrane remarkably alleviates material volume expansion during charge and discharge and facilitates the penetration of the liquid electrolyte; (b) CNTs provide a long-range continuous electrical percolated framework, resulting in the fast charge diffusion kinetics of the $H_{0.08}MnO_2{\cdot}0.7H_2O$/MWCNT membrane cathode; (c) the absence of any organic polymer as a binder avoids the adsorption between the high charge density of Zn^{2+} and the polarizing bonds in the polymeric binder, resulting in the enhancement of Zn^{2+} mobility during the charge/discharge processes.

Wearable, Paper-Like Zn//$H_{0.08}MnO_2{\cdot}0.7H_2O$/MWCNT Battery. Finally, considering the continuous demand for the flexible wearable devices, our $H_{0.08}MnO_2{\cdot}0.7H_2O$/MWCNT membrane is further assembled into flexible, foldable cells to broaden its application. As shown in Figure 7a, the paper-thin ZIB was assembled with the $H_{0.08}MnO_2{\cdot}0.7H_2O$/MWCNT

https://doi.org/10.1021/acsaem.1c00464
ACS Appl. Energy Mater. 2021, 4, 4138–4149

cathode and 2 M $ZnSO_4$ + 0.2 M $MnSO_4$ aqueous solution electrolyte, a positron emission tomography nonwoven fabric separator (~80 μm), and a flexible Zn foil anode. Figure 7b delivers the GDC curves of a single ZIB and two ZIBs connected in series having a rather steady charge/discharge platform in the voltage intervals of 1−1.9 and 2−3.8 V, respectively. The assembled two-charged ZIBs connected in series could be easily wrapped around the wrist to light up a red light-emitting diode (LED) indicator (Figure 7c). Furthermore, when the battery was bent from 0 to 180° and then returned to the initial state, the LED was observed to illuminate continuously (Figure 7d−i), demonstrating its excellent flexibility and potential for promising applications in wearable electrics.

CONCLUSIONS

In conclusion, we demonstrated the excellent zinc-ion-storage behavior of $H_{0.08}MnO_2{\cdot}0.7H_2O$ birnessite nanobelts for the first time in a macroporous, freestanding $H_{0.08}MnO_2{\cdot}0.7H_2O$/MWCNT membrane. This macroporous membrane cathode delivers a high Zn^{2+} diffusion coefficient of ~8.18×10^{-14} cm^2 s^{-1}, specific capacity of 277.6 mA h g^{-1} at 0.2 A g^{-1}, and excellent cycling stability over 1000 cycles at 3.0 A g^{-1}. The energy density of the Zn//$H_{0.08}MnO_2{\cdot}0.7H_2O$/MWCNT battery reaches up to 368.3 W h·kg^{-1} at a power density of 300 W·kg^{-1}. Soft-packaged ZIBs assembled with the membrane cathode show stable electrochemical performance at different bending states toward flexible wearable electrics applications. Our study not only revealed that the proton-type birnessite $H_{0.08}MnO_2{\cdot}0.7H_2O$ is a very promising and robust cathode material for aqueous ZIBs but also developed a macropore-assisted binder-free strategy to realize next-generation energy-storage devices from layered nanostructures with a high aspect ratio. This strategy can be potentially applied to robust electrodes of other multivalent metal-ion (Al^{3+}, Mg^{2+}, Ca^{2+}, etc.) batteries.

EXPERIMENTAL DETAILS

Synthesis of $H_{0.08}MnO_2{\cdot}0.7H_2O$ Nanobelts. 6 mmol $KMnO_4$ (GR, Sinopharm chemical reagent Co., Ltd. (SCRC)) was dissolved in 137.5 mL Milli-Q water (18.2 MΩ·cm) to form a solution, and 3 mol KOH (AR, SCRC) was added to this solution in two batches under vigorous stirring. Then, 20 mL of 0.6 M $MnCl_2$ (AR, SCRC) aqueous solution was quickly introduced into the above mixed solution and stirred for 2 h to get a uniform precursor solution. This resulting solution was hydrothermally reacted at 175 °C for 72 h. The manganese oxide precipitate was rinsed thoroughly with Milli-Q water to neutral pH, after which 0.25 mol $(NH_4)_2S_2O_8$ (AR, SCRC) was dispersed into the neutral solution in a three-necked flask, and the mixture was stirred under 60 °C for 3 h (repeated three times) and then filtered and washed by Milli-Q water to get the $H_{0.08}MnO_2{\cdot}0.7H_2O$ aqueous suspension. The ideal reaction mechanism in the synthesis is expressed as

$$8K_{0.33}MnO_2{\cdot}0.5H_2O + (NH_4)_2S_2O_8 + 2.59H_2O \rightarrow 8H_{0.08}MnO_2{\cdot}0.7H_2O + K_2SO_4 + (NH_4)2SO_4 + 0.64KOH$$

Finally, the $H_{0.08}MnO_2{\cdot}0.7H_2O$ suspension was freeze-dried under 5 bar at −50 °C for 48 h to obtain the $H_{0.08}MnO_2{\cdot}0.7H_2O$ powder.

Construction of $H_{0.08}MnO_2{\cdot}0.7H_2O$/MWCNT Hybrid Membrane. 7.5 mL of the $H_{0.08}MnO_2{\cdot}0.7H_2O$ aqueous solution (4.25 mg mL^{-1}) was added to 15 mL of carbon nanotube (CNT, Tanfeng Technology Co., Ltd.) and NMP (AR, SCRC) suspension (0.5 mg mL^{-1}), which was mechanically ground for 15 min and ultrasonically treated for another 1 h. After the treatment, a homogeneous $H_{0.08}MnO_2{\cdot}0.7H_2O$ belts/CNT composite suspension was readily formed. Then, the $H_{0.08}MnO_2{\cdot}0.7H_2O$ nanobelts and CNTs agglomerated together to generate a porous framework membrane by the vacuum-assisted filtration method. Finally, the membrane was washed three times with Milli-Q water and dried naturally in air. It is noticed that the optimal initial content of CNTs in the composited $H_{0.08}MnO_2{\cdot}0.7H_2O$ hybrid membrane is ~20% because a higher mass ratio of CNTs drastically affected the formation of $H_{0.08}MnO_2{\cdot}0.7H_2O$ while a lower ratio affected the electronic conductivity. The $H_{0.08}MnO_2{\cdot}0.7H_2O$/MWCNT membrane was punched into circular pieces (Φ = 15 mm, mass loading ~2.3 mg cm^{-2}) and directly utilized as a cathode.

Material Characterization. Powder XRD analysis was performed to investigate the crystal structure (Bruker D8-A25 diffractometer using Cu Kα radiation (λ = 1.5406 Å); scan rate was 2° min^{-1}). TGA (30−900 °C, heating rate 10 °C min^{-1}, air flow 50 mL min^{-1}) was employed to explore the sample's thermal behavior. An AUTO tensile tester (Labthink, XLW (PC)) was utilized to measure the tensile strength of the $H_{0.08}MnO_2{\cdot}0.7H_2O$/MWCNT membrane. TEM (FEI TECNAI G^2 S-TWIN), SAED, and field emission scanning electron microscopy (FEI Navo Nano SEM 450) were performed to characterize the sample's morphology. XPS (PerkinElmer PHI 5000C ESCA, with Mg Kα radiation, standard signal: C 1s peak 284.6 eV) analysis was done to investigate the elemental distribution and chemical components. A zeta-potential tester (Zetasizer Nano ZS90) was used to characterize the surface charge state of the nanobelts dispersed in solvents. An electric resistance tester (Fluke 87-V/C) was used to characterize the electric resistance of the $H_{0.08}MnO_2{\cdot}0.7H_2O$/MWCNT composite membrane with various MWCNT contents.

Electrochemical Measurements. A freestanding $H_{0.08}MnO_2{\cdot}0.7H_2O$/MWCNT membrane was employed as the cathode of coin-type cells directly. For the powder sample, the cathode was prepared by mixing the freeze-dried powder:Ketjen black:PVDF (mass ratio = 7:2:1) with NMP. Then, the homogeneous slurry was coated onto 304 stainless-steel foil and dried under vacuum at 80 °C overnight. Finally, the coated foil was punched into circular pieces (Φ = 15 mm, mass loading ~ 2 mg cm^{-2}) for the assembly of coin-type cells. The electrochemical performances of the assembled coin-type Zn//$H_{0.08}MnO_2{\cdot}0.7H_2O$/MWCNT membrane and Zn//$H_{0.08}MnO_2{\cdot}0.7H_2O$/PVDF powder cells were evaluated with the LAND battery cycle system (Wuhan LAND Electronics Co., Ltd., China) in the voltage range of 1−1.9 V at ambient conditions. The high-purity Zn foils (thickness of 30 μm; Tengfeng Metal Materials Ltd.), Whatman GF (thickness of 350 μm), and 2 M $ZnSO_4$ (SCRC, 99.995%)/0.2 M $MnSO_4$ (SCRC, AR) aqueous solution were used as the anode, separator, and electrolyte, respectively. The cycling performance was measured at 0.2 and 3.0 A g^{-1}, respectively. The rate capability of the ZIBs was tested in the range from 0.2 to 7 A g^{-1}. GITT test was performed at 0.1 A g^{-1} for 30 min, followed by a relaxation period of 1 h. CV (in the voltage range of 1−1.9 V) and EIS (in the frequency range of 10 mHz−1 MHz) tests were performed on an electrochemical workstation (CHI660e). All cells were aged for 12 h prior to any electrochemical test to ensure that the electrolyte was well absorbed by the separator and the electrode.

Calculation Methods. The capacity contribution can be clarified by separating the controlled effects of capacitive and diffusion capacities. Generally, the capacitive contribution parts can be distinguished by the following modified equations

$$I = av^b \quad (1)$$

$$I = I_{\text{capacitive}} + I_{\text{diffusion}} = k_1\nu + k_2\nu^{1/2} \quad (2)$$

$$\frac{I}{\nu^{1/2}} = I_{\text{capacitive}} + I_{\text{diffusion}} = k_1\nu^{1/2} + k_2 \quad (3)$$

where I represents the peak current density; ν represents the scan rate; and k_1 and k_2 represent the constant factors of the current contributions from the pseudocapacitive-controlled and diffusion-controlled effects, respectively.

https://doi.org/10.1021/acsaem.1c00464
ACS Appl. Energy Mater. 2021, 4, 4138−4149

The diffusion coefficients ($cm^2\ s^{-1}$) of the Zn ion and proton at the discharge platform can be calculated by the following equation

$$D = \frac{R^2T^2}{2A^2\ n^4F^4C^2\sigma^2} \tag{4}$$

where the constant factors of gas constant (R), the experimental temperature (T), and the Faraday constant (F) are 8.314 J K^{-1} mol^{-1}, 298 K, and 96,500 C mol^{-1}, respectively. Moreover, the adjustable factors of surface area of the electrode are represented by A, the number of electrons transferred per mole of electrode involved in the reaction by n, the concentration of insertion ion in the cathode by C, and the slope value of the line Z' versus $\omega^{-1/2}$ by σ.

The diffusion coefficient (D_{GITT}, $cm^2\ s^{-1}$) for the zinc ion in the $H_{0.08}MnO_2{\cdot}0.7H_2O$/MWCNT membrane cathode can be calculated by the following equation

$$D_{GITT} = \frac{4}{\pi\tau}\left(\frac{nV}{A}\right)^2\left(\frac{\Delta Es}{\Delta E\tau}\right)^2 \qquad (t \ll L^2/D) \tag{5}$$

where the duration time of current pulse is represented by τ (s), the mole number of the active material by n, the contacting surface area by A (cm^2), the molar volume by V (cm^3 mol^{-1}), and the molecular weight by M (g mol^{-1}); ΔE is the voltage change caused by the current pulse and the galvanostatic charge/discharge.

The energy density (E, W h kg^{-1}) and average power density (P, W kg^{-1}) of our membrane cathode-based ZIBs can be calculated by the following equations

$$E = \int_{V_a}^{V_b} C(V)\mathrm{d}V \tag{6}$$

$$P = E/t \tag{7}$$

where C (mA h g^{-1}) is the specific capacity of the battery; V_a and V_b are the lower and upper limits of voltage during the discharge procedure, respectively; and t is the discharge time (h). The values of E and P were calculated based on the active material $H_{0.08}MnO_2{\cdot}0.7H_2O$ only.

■ ASSOCIATED CONTENT

Supporting Information

The Supporting Information is available free of charge at https://pubs.acs.org/doi/10.1021/acsaem.1c00464.

Zeta potential of the $H_{0.08}MnO_2{\cdot}0.7H_2O$ suspension; flexibility of the $H_{0.08}MnO_2{\cdot}0.7H_2O$/MWCNT hybrid membrane; XRD patterns and SEM images of the pure $H_{0.08}MnO_2{\cdot}0.7H_2O$ membrane; XPS spectra, tensile strength, and thermal stability of the $H_{0.08}MnO_2{\cdot}0.7H_2O$/MWCNT membrane; GDC curves of the $H_{0.08}MnO_2{\cdot}0.7H_2O$/MWCNT membrane-based ZIBs at various cycle numbers/current densities; cycle performance (0.2 A g^{-1}) of $H_{0.08}MnO_2{\cdot}0.7H_2O$-based ZIBs with/without PVDF; cycle performance of $H_{0.08}MnO_2{\cdot}0.7H_2O$/WMCNT-based ZIBs with/without $MnSO_4$; and Nyquist spectrum of freeze-dried $H_{0.08}MnO_2{\cdot}0.7H_2O$ powder electrodes (PDF)

■ AUTHOR INFORMATION

Corresponding Author

Linfeng Hu − *Department of Materials Science, Fudan University, Shanghai 200433, P. R. China;* orcid.org/0000-0002-0640-508X; Email: linfenghu@fudan.edu.cn

Authors

Yanan Wang − *Department of Materials Science, Fudan University, Shanghai 200433, P. R. China*

Fei Ye − *School of Materials Science and Engineering, Southeast University, Nanjing 211189, P. R. China*

Zeyi Wu − *Department of Materials Science, Fudan University, Shanghai 200433, P. R. China*

Le Jiang − *Department of Materials Science, Fudan University, Shanghai 200433, P. R. China*

Lin Zhang − *Department of Materials Science, Fudan University, Shanghai 200433, P. R. China*

Complete contact information is available at: https://pubs.acs.org/10.1021/acsaem.1c00464

Notes

The authors declare no competing financial interest.

■ ACKNOWLEDGMENTS

This work was financially supported by the National Natural Science Foundation of China (nos. 51872051, 51731004), the Science and Technology Committee of Shanghai Municipality (18520723100), and the Fundamental Research Funds for the Central Universities.

■ REFERENCES

(1) Nam, K. W.; Park, S. S.; dos Reis, R.; Dravid, V. P.; Kim, H.; Mirkin, C. A.; Stoddart, J. F. Conductive 2D Metal-organic Framework for High-performance Cathodes in Aqueous Rechargeable Zinc Batteries. *Nat. Commun.* **2019**, *10*, 4948.

(2) Pan, H.; Shao, Y.; Yan, P.; Cheng, Y.; Han, K. S.; Nie, Z.; Wang, C.; Yang, J.; Li, X.; Bhattacharya, P.; Mueller, K. T.; Liu, J. Reversible Aqueous Zinc/Manganese Oxide Energy Storage from Conversion Reactions. *Nat. Energy* **2016**, *1*, 16039.

(3) Mathew, V.; Sambandam, B.; Kim, S.; Kim, S.; Park, S.; Lee, S.; Alfaruqi, M. H.; Soundharrajan, V.; Islam, S.; Putro, D. Y.; Hwang, J.-Y.; Sun, Y.-K.; Kim, J. Manganese and Vanadium Oxide Cathodes for Aqueous Rechargeable Zinc-Ion Batteries: A Focused View on Performance, Mechanism, and Developments. *ACS Energy Lett.* **2020**, *5*, 2376−2400.

(4) Zampardi, G.; La Mantia, F. Prussian Blue Analogues as Aqueous Zn-ion Batteries Electrodes: Current Challenges and Future Perspectives. *Curr. Opin. Electrochem.* **2020**, *21*, 84−92.

(5) Demir-Cakan, R.; Palacin, M. R.; Croguennec, L. Rechargeable Aqueous Electrolyte Batteries: from Univalent to Multivalent Cation Chemistry. *J. Mater. Chem. A* **2019**, *7*, 20519−20539.

(6) Shin, J.; Seo, J. K.; Yaylian, R.; Huang, A.; Meng, Y. S. A review on mechanistic understanding of MnO_2 in aqueous electrolyte for electrical energy storage systems. *Int. Mater. Rev.* **2020**, *65*, 356−387.

(7) Blanc, L. E.; Kundu, D.; Nazar, L. F. Scientific Challenges for the Implementation of Zn-Ion Batteries. *Joule* **2020**, *4*, 771−799.

(8) Islam, S.; Alfaruqi, M. H.; Mathew, V.; Song, J.; Kim, S.; Kim, S.; Jo, J.; Baboo, J. P.; Pham, D. T.; Putro, D. Y.; Sun, Y.-K.; Kim, J. Facile synthesis and the exploration of the zinc storage mechanism of β-MnO_2 nanorods with exposed (101) planes as a novel cathode material for high performance eco-friendly zinc-ion batteries. *J. Mater. Chem. A* **2017**, *5*, 23299−23309.

(9) Alfaruqi, M. H.; Mathew, V.; Gim, J.; Kim, S.; Song, J.; Baboo, J. P.; Choi, S. H.; Kim, J. Electrochemically Induced Structural Transformation in a γ-MnO_2 Cathode of a High Capacity Zinc-Ion Battery System. *Chem. Mater.* **2015**, *27*, 3609−3620.

(10) Yadav, G. G.; Cho, J.; Turney, D.; Hawkins, B.; Wei, X.; Huang, J.; Banerjee, S.; Nyce, M. Going beyond Intercalation Capacity of Aqueous Batteries by Exploiting Conversion Reactions of Mn and Zn electrodes for Energy-Dense Applications. *Adv. Energy Mater.* **2019**, *9*, 1902270.

(11) Lee, J.-W.; Seo, S.-D.; Kim, D.-W. Comparative study on ternary spinel cathode Zn-Mn-O microspheres for aqueous rechargeable zinc-ion batteries. *J. Alloys Compd.* **2019**, *800*, 478−482.

(12) Ko, J. S.; Sassin, M. B.; Parker, J. F.; Rolison, D. R.; Long, J. W. Combining battery-like and pseudocapacitive charge storage in 3D MnO_x@carbon electrode architectures for zinc-ion cells. *Sustainable Energy Fuels* **2018**, *2*, 626−636.
(13) Kataoka, F.; Ishida, T.; Nagita, K.; Kumbhar, V.; Yamabuki, K.; Nakayama, M. Cobalt-Doped Layered MnO_2 Thin Film Electrochemically Grown on Nitrogen-Doped Carbon Cloth for Aqueous Zinc-Ion Batteries. *ACS Appl. Energy Mater.* **2020**, *3*, 4720−4726.
(14) Zhang, N.; Cheng, F.; Liu, J.; Wang, L.; Long, X.; Liu, X.; Li, F.; Chen, J. Rechargeable Aqueous Zinc-Manganese Dioxide Batteries with High Energy and Power Densities. *Nat. Commun.* **2017**, *8*, 405.
(15) Alfaruqi, M. H.; Islam, S.; Gim, J.; Song, J.; Kim, S.; Pham, D. T.; Jo, J.; Xiu, Z.; Mathew, V.; Kim, J. A high surface area tunnel-type α-MnO_2 nanorod cathode by a simple solvent-free synthesis for rechargeable aqueous zinc-ion batteries. *Chem. Phys. Lett.* **2016**, *650*, 64−68.
(16) Housel, L. M.; Wang, L.; Abraham, A.; Huang, J.; Renderos, G. D.; Quilty, C. D.; Brady, A. B.; Marschilok, A. C.; Takeuchi, K. J.; Takeuchi, E. S. Investigation of α-MnO_2 Tunneled Structures as Model Cation Hosts for Energy Storage. *Acc. Chem. Res.* **2018**, *51*, 575−582.
(17) Han, S.-D.; Kim, S.; Li, D.; Petkov, V.; Yoo, H. D.; Phillips, P. J.; Wang, H.; Kim, J. J.; More, K. L.; Key, B.; Klie, R. F.; Cabana, J.; Stamenkovic, V. R.; Fister, T. T.; Markovic, N. M.; Burrell, A. K.; Tepavcevic, S.; Vaughey, J. T. Mechanism of Zn Insertion into Nanostructured δ-MnO_2: A Nonaqueous Rechargeable Zn Metal Battery. *Chem. Mater.* **2017**, *29*, 4874−4884.
(18) Sada, K.; Senthilkumar, B.; Barpanda, P. Cryptomelane $K_{1.33}Mn_8O_{16}$ as a cathode for rechargeable aqueous zinc-ion batteries. *J. Mater. Chem. A* **2019**, *7*, 23981−23988.
(19) Yadav, G. G.; Gallaway, J. W.; Turney, D. E.; Nyce, M.; Huang, J.; Wei, X.; Banerjee, S. Regenerable Cu-intercalated MnO_2 Layered Cathode for Highly Cyclable Energy Dense Batteries. *Nat. Commun.* **2017**, *8*, 14424.
(20) Liu, Z.; Ma, R.; Ebina, Y.; Takada, K.; Sasaki, T. Synthesis and Delamination of Layered Manganese Oxide Nanobelts. *Chem. Mater.* **2007**, *19*, 6504−6512.
(21) Lee, B.; No, W. J.; Oh, S. H. Unravelling the Role of Interfacial Chemistry Evolution in the Kinetics of Zinc Insertion into Chevrel Phase. *J. Power Sources* **2020**, *478*, 229086.
(22) Kim, H. J.; Jo, J. H.; Choi, J. U.; Voronina, N.; Myung, S.-T. KV_3O_8 with a large interlayer as a viable cathode material for zinc-ion batteries. *J. Power Sources* **2020**, *478*, 229072.
(23) Zhang, Y.; Xu, G.; Liu, X.; Wei, X.; Cao, J.; Yang, L. Scalable In Situ Reactive Assembly of Polypyrrole-Coated MnO_2 Nanowire and Carbon Nanotube Composite as Freestanding Cathodes for High Performance Aqueous Zn-Ion Batteries. *ChemElectroChem* **2020**, *7*, 2762−2770.
(24) Shi, F.; Mang, C.; Liu, H.; Dong, Y. Flexible and high-energy-density Zn/MnO_2 batteries enabled by electrochemically exfoliated graphene nanosheets. *New J. Chem.* **2020**, *44*, 653−657.
(25) Wang, S.; Wang, Q.; Zeng, W.; Wang, M.; Ruan, L.; Ma, Y. A New Free-Standing Aqueous Zinc-Ion Capacitor Based on MnO_2−CNTs Cathode and MXene Anode. *Nano-Micro Lett.* **2019**, *11*, 70.
(26) Wang, Y.; Wu, Z.; Jiang, L.; Tian, W.; Zhang, C.; Cai, C.; Hu, L. A long-lifespan, flexible zinc-ion secondary battery using a paper-like cathode from single-atomic layer MnO_2 nanosheets. *Nanoscale Adv.* **2019**, *1*, 4365−4372.
(27) Yang, W.; Zhang, Y.; Zhang, Y.; Deng, W.; Fang, X. Transparent Schottky Photodiode Based on AgNi NWs/$SrTiO_3$ Contact with an Ultrafast Photoresponse to Short-Wavelength Blue Light and UV-Shielding Effect. *Adv. Funct. Mater.* **2019**, *29*, 1905923.
(28) Dwivedi, N.; Yeo, R. J.; Satyanarayana, N.; Kundu, S.; Tripathy, S.; Bhatia, C. S. Understanding the Role of Nitrogen in Plasma-Assisted Surface Modification of Magnetic Recording Media with and without Ultrathin Carbon Overcoats. *Sci. Rep.* **2015**, *5*, 7772.
(29) Zhao, C.; Yu, C.; Zhang, M.; Huang, H.; Li, S.; Han, X.; Liu, Z.; Yang, J.; Xiao, W.; Liang, J.; Sun, X.; Qiu, J. Ultrafine MoO_2-Carbon Microstructures Enable Ultralong-Life Power-Type Sodium Ion Storage by Enhanced Pseudocapacitance. *Adv. Energy Mater.* **2017**, *7*, 1602880.
(30) Fu, Y.; Wei, Q.; Zhang, G.; Wang, X.; Zhang, J.; Hu, Y.; Wang, D.; Zuin, L.; Zhou, T.; Wu, Y.; Sun, S. High-Performance Reversible Aqueous Zn-Ion Battery Based on Porous MnO_x Nanorods Coated by MOF-Derived N-Doped Carbon. *Adv. Energy Mater.* **2018**, *8*, 1801445.
(31) Jiang, Y.; Ba, D.; Li, Y.; Liu, J. Noninterference Revealing of "Layered to Layered" Zinc Storage Mechanism of δ-MnO_2 toward Neutral Zn-Mn Batteries with Superior Performance. *Adv. Sci.* **2020**, *7*, 1902795.
(32) Lian, S.; Sun, C.; Xu, W.; Huo, W.; Luo, Y.; Zhao, K.; Yao, G.; Xu, W.; Zhang, Y.; Li, Z.; Yu, K.; Zhao, H.; Cheng, H.; Zhang, J.; Mai, L. Built-in oriented electric field facilitating durable ZnMnO_2 battery. *Nano Energy* **2019**, *62*, 79−84.
(33) Lv, P.; Feng, Y. Y.; Li, Y.; Feng, W. Carbon fabric-aligned carbon nanotube/MnO_2/conducting polymers ternary composite electrodes with high utilization and mass loading of MnO_2 for super-capacitors. *J. Power Sources* **2012**, *220*, 160−168.
(34) Zhai, X.-Z.; Qu, J.; Hao, S.-M.; Jing, Y.-Q.; Chang, W.; Wang, J.; Li, W.; Abdelkrim, Y.; Yuan, H.; Yu, Z.-Z. Layered Birnessite Cathode with a Displacement/Intercalation Mechanism for High-Performance Aqueous Zinc-Ion Batteries. *Nano-Micro Lett.* **2020**, *12*, 56.
(35) Dhiman, A.; Ivey, D. G. Electrodeposited Manganese Oxide on Carbon Paper for Zinc-Ion Battery Cathodes. *Batteries Supercaps* **2020**, *3*, 293−305.
(36) Fenta, F. W.; Olbasa, B. W.; Tsai, M.-C.; Weret, M. A.; Zegeye, T. A.; Huang, C.-J.; Huang, W.-H.; Zeleke, T. S.; Sahalie, N. A.; Pao, C.-W.; Wu, S.-h.; Su, W.-N.; Dai, H.; Hwang, B. J. Electrochemical transformation reaction of Cu-MnO in aqueous rechargeable zinc-ion batteries for high performance and long cycle life. *J. Mater. Chem. A* **2020**, *8*, 17595−17607.
(37) Khamsanga, S.; Pornprasertsuk, R.; Yonezawa, T.; Mohamad, A. A.; Kheawhom, S. δ-MnO_2 Nanoflower/graphite Cathode for Rechargeable Aqueous Zinc Ion Batteries. *Sci. Rep.* **2019**, *9*, 8441.
(38) Long, J.; Yang, F.; Cuan, J.; Wu, J.; Yang, Z.; Jiang, H.; Song, R.; Song, W.; Mao, J.; Guo, Z. Boosted Charge Transfer in Twinborn α-(Mn_2O_3-MnO_2) Heterostructures: Toward High-Rate and Ultra-long-Life Zinc-Ion Batteries. *ACS Appl. Mater. Interfaces* **2020**, *12*, 32526−32535.
(39) Zeng, X.; Liu, J.; Mao, J.; Hao, J.; Wang, Z.; Zhou, S.; Ling, C. D.; Guo, Z. Toward a Reversible Mn^{4+}/Mn^{2+} Redox Reaction and Dendrite-Free Zn Anode in Near-Neutral Aqueous Zn/MnO_2 Batteries via Salt Anion Chemistry. *Adv. Energy Mater.* **2020**, *10*, 1904163.
(40) Hao, J.; Li, X.; Zeng, X.; Li, D.; Mao, J.; Guo, Z. Deeply understanding the Zn anode behaviour and corresponding improvement strategies in different aqueous Zn-based batteries. *Energy Environ. Sci.* **2020**, *13*, 3917−3949.
(41) He, P.; Yan, M.; Zhang, G.; Sun, R.; Chen, L.; An, Q.; Mai, L. Layered VS_2 Nanosheet-Based Aqueous Zn Ion Battery Cathode. *Adv. Energy Mater.* **2017**, *7*, 1601920.
(42) Jiang, B.; Xu, C.; Wu, C.; Dong, L.; Li, J.; Kang, F. Manganese Sesquioxide as Cathode Material for Multivalent Zinc Ion Battery with High Capacity and Long Cycle Life. *Electrochim. Acta* **2017**, *229*, 422−428.
(43) Hu, P.; Yan, M.; Zhu, T.; Wang, X.; Wei, X.; Li, J.; Zhou, L.; Li, Z.; Chen, L.; Mai, L. Zn/V_2O_5 Aqueous Hybrid-Ion Battery with High Voltage Platform and Long Cycle Life. *ACS Appl. Mater. Interfaces* **2017**, *9*, 42717−42722.
(44) Hao, J.; Mou, J.; Zhang, J.; Dong, L.; Liu, W.; Xu, C.; Kang, F. Electrochemically induced spinel-layered phase transition of Mn_3O_4 in high performance neutral aqueous rechargeable zinc battery. *Electrochim. Acta* **2018**, *259*, 170−178.
(45) Soundharrajan, V.; Sambandam, B.; Kim, S.; Mathew, V.; Jo, J.; Kim, S.; Lee, J.; Islam, S.; Kim, K.; Sun, Y.-K.; Kim, J. Aqueous Magnesium Zinc Hybrid Battery: An Advanced High-Voltage and

https://doi.org/10.1021/acsaem.1c00464
ACS Appl. Energy Mater. 2021, 4, 4138−4149

High-Energy $MgMn_2O_4$ Cathode. *ACS Energy Lett.* **2018**, *3*, 1998−2004.
(46) Zhang, L.; Chen, L.; Zhou, X.; Liu, Z. Towards High-Voltage Aqueous Metal-Ion Batteries Beyond 1.5 V: The Zinc/Zinc Hexacyanoferrate System. *Adv. Energy Mater.* **2015**, *5*, 1400930.
(47) Lee, J.; Ju, J. B.; Cho, W. I.; Cho, B. W.; Oh, S. H. Todorokite-type MnO_2 as a zinc-ion intercalating material. *Electrochim. Acta* **2013**, *112*, 138−143.
(48) Wu, Z.; Wang, Y.; Zhang, L.; Jiang, L.; Tian, W.; Cai, C.; Price, J.; Gu, Q.; Hu, L. A Layered $Zn_{0.4}VOPO_4{\cdot}0.8H_2O$ Cathode for Robust and Stable Zn Ion Storage. *ACS Appl. Energy Mater.* **2020**, *3*, 3919−3927.
(49) Alfaruqi, M. H.; Gim, J.; Kim, S.; Song, J.; Pham, D. T.; Jo, J.; Xiu, Z.; Mathew, V.; Kim, J. A layered δ-MnO_2 nanoflake cathode with high zinc-storage capacities for eco-friendly battery applications. *Electrochem. Commun.* **2015**, *60*, 121−125.
(50) Zhang, B.; Liu, Y.; Wu, X.; Yang, Y.; Chang, Z.; Wen, Z.; Wu, Y. An aqueous rechargeable battery based on zinc anode and $Na_{0.95}MnO_2$. *Chem. Commun.* **2014**, *50*, 1209−1211.
(51) Ming, F.; Liang, H.; Lei, Y.; Kandambeth, S.; Eddaoudi, M.; Alshareef, H. N. Layered $Mg_xV_2O_5{\cdot}nH_2O$ as Cathode Material for High-Performance Aqueous Zinc Ion Batteries. *ACS Energy Lett.* **2018**, *3*, 2602−2609.
(52) Alfaruqi, M. H.; Islam, S.; Putro, D. Y.; Mathew, V.; Kim, S.; Jo, J.; Kim, S.; Sun, Y.-K.; Kim, K.; Kim, J. Structural transformation and electrochemical study of layered MnO_2 in rechargeable aqueous zinc-ion battery. *Electrochim. Acta* **2018**, *276*, 1−11.
(53) Jiao, Y.; Kang, L.; Berry-Gair, J.; McColl, K.; Li, J.; Dong, H.; Jiang, H.; Wang, R.; Corà, F.; Brett, D. J. L.; He, G.; Parkin, I. P. Enabling stable MnO_2 matrix for aqueous zinc-ion battery cathodes. *J. Mater. Chem. A* **2020**, *8*, 22075−22082.
(54) Huang, J.; Wang, Z.; Hou, M.; Dong, X.; Liu, Y.; Wang, Y.; Xia, Y. Polyaniline-intercalated Manganese Dioxide Nanolayers as a High-performance Cathode Material for an Aqueous Zinc-ion Battery. *Nat. Commun.* **2018**, *9*, 2906.
(55) Sun, X.; Duffort, V.; Mehdi, B. L.; Browning, N. D.; Nazar, L. F. Investigation of the Mechanism of Mg Insertion in Birnessite in Nonaqueous and Aqueous Rechargeable Mg-Ion Batteries. *Chem. Mater.* **2016**, *28*, 534−542.
(56) Xia, C.; Guo, J.; Lei, Y.; Liang, H.; Zhao, C.; Alshareef, H. N. Rechargeable Aqueous Zinc-Ion Battery Based on Porous Framework Zinc Pyrovanadate Intercalation Cathode. *Adv. Mater.* **2018**, *30*, 1705580.
(57) Deng, Z.; Huang, J.; Liu, J.; Ren, L.; Zhu, L.; Xiao, X.; Tan, M. β-MnO_2 nanolayer coated on carbon cloth as a high-activity aqueous zinc-ion battery cathode with high-capacity and long-cycle-life. *Mater. Lett.* **2019**, *248*, 207−210.
(58) Wang, J.; Wang, J.-G.; Liu, H.; Wei, C.; Kang, F. Zinc ion stabilized MnO_2 nanospheres for high capacity and long lifespan aqueous zinc-ion batteries. *J. Mater. Chem. A* **2019**, *7*, 13727−13735.

https://doi.org/10.1021/acsaem.1c00464
ACS Appl. Energy Mater. 2021, 4, 4138−4149